ORIGINAL RESEARCH PAPERS

Towards reduced ultrasound localization microscopy acquisition times by uncoupling a bi-disperse microbubble population

GIULIA TUCCIO[1], LISA TE WINKEL[2], CORINNE BRUGGEMAN[2], WIM VAN HOEVE[2], LIBERTARIO DEMI[1]

[1]Department of Information Engineering and Computer Science, University of Trento, Trento, Italy; [2]Solstice Pharmaceuticals, Enschede, The Netherlands

ABSTRACT

Background: Ultrasound Localization Microscopy (ULM) is a milestone in the medical vascular imaging context, enabling the precise characterization of microvascular structures using ultrasound imaging. By accurately localizing contrast microbubbles (MBs) flowing in the circulatory system, ULM generates microresolved vascular images, overcoming the ultrasonic diffraction limit. However, as ULM relies on precise localization and tracking of individual MBs, high MB concentrations yield to increased localization errors and, ultimately, ULM failure. This constraint limits ULM to low MB concentrations, resulting in long acquisition times that pose challenges in clinical settings.
Methods: Here, we show the feasibility of uncoupling a bi-disperse MB population, composed of two monodisperse MB populations. The uncoupling is performed through a signal processing pipeline that exploits the strong nonlinear response of MBs having resonance frequency tuned with the transmission frequency. After uncoupling, ULM density and velocity flow maps are generated.
Results: Density and velocity maps are generated after uncoupling, when injecting the bi-disperse population individually and simultaneously in a vascular 3D-printed phantom. Furthermore, density maps generated after uncoupling are compared with the one obtained using standard ULM. Results demonstrate the capability of the proposed uncoupling pipeline to separate the bi-disperse population.

Received: 17 October 2025 | Accepted: 6 February 2026
Correspondence: Prof. Libertario Demi / Univerisity of Trento, Via Sommarive, 38123 Trento, Italy /
E-mail: Libertario.demi@unitn.it - ORCID: 0000-0002-0635-2133

Conclusions: This work presents a signal processing pipeline to uncouple a bidisperse MB population, formed by two monodisperse MB populations. are validated in a 3D-printed phantom and demonstrate the feasibility of the uncoupling which, in turn, would enable higher concentrations and reduce acquisition times for micro-vascular imaging.

Key words: ultrasound localization microscopy, ultrasound contrast agents, microbubble uncoupling, monodisperse microbubble population, signal processing

Background

Ultrasound imaging is extensively used in the clinical context owing to low cost, nontoxicity and ease of use (1, 2). Because of these features, it is applied in various medical fields, including maternity, gynaecology, urology, cerebrovascular examinations, and intraoperative procedures (3). Despite its broad range of applications, imaging the microvascular bed is challenging for ultrasound imaging. Ultrasound is not able, per se, to resolve vascular structures smaller than the diffraction limit, which is half-awavelength (for instance, a 5 MHz ultrasound wave in tissue has a 300 μm wavelength) (1, 4). Micro-vascular structures reach down to 10 μm (5), thus are indistinguishable to ultrasound (4, 5). In an effort to break the ultrasound resolution limit, Couture et al. (4) and Siepmann et al. (6) proposed to accumulate localizations of injected microbubbles (MBs) to enhance microvascular imaging spatial resolution. These works gave birth to Ultrasound Localization Microscopy (ULM). ULM combines the ultrasound-based medical imaging benefits, enabling the visualization of static and dynamic properties of microvascular structures (4, 6). The spatial resolution of ULM-generated images ranges from a fifth to a tenth of the wavelength (8). ULM exploits the strong acoustic scattering signals produced by gas-filled contrast microbubbles, whose dimension is substantially smaller than the typical ultrasound wavelength (9). While the diffraction limit dictates the resolution of MBs' ultrasound images, which can be estimated through a Point Spread Function (PSF) (see Figure 1a as an example), individual MB can be localized with precision below the diffraction limit (4, 6, 10). By tracking the localized MBs through a sequence of ultrasound images, ULM generates the micro-resolved density maps. These tracks also provide dynamic information on vascular structures, such as flow velocity and direction, allowing ULM to capture structural and functional information (1, 4, 6, 11, 12). The level of detail provided by ULM's density and velocity maps has the potential to be a powerful tool in the clinical context. Specifically, ULM preserves the benefits of ultrasound (such as safety, cost-efficiency, and non-toxicity) while offering resolution beyond the diffraction limit at clinically relevant depth. Furthermore, ULM can be implemented as a post-processing step, making it easy to integrate into clinical practice to provide a more comprehensive understanding of the circulatory system and its functioning. ULM could also help understand the correlation between microvascular alterations and diseases like cancer, diabetes, and arteriosclerosis, which is valuable for diagnostic and therapeutic monitoring (1, 4, 3–15). Although the technique has been present for more than a decade, its clinical applications are limited by various factors, including long acquisition times, high temporal resolution and MBs' inaccurate localization and tracking due to noise and motion (1, 2, 11). This study addresses the ULM's long acquisition time constraint. MB localization precision is crucial for the quality of the reconstructed images. However, ULM requires isolated MB signals for accurate localization. Failing to ensure MB sparsity would cause overlapping MB PSF in ultrasound images. Because localization errors related to such situations are high, these MBs

are usually excluded from the analysis. As a result, ULM often operates with low MB concentrations, leading to long acquisition times to accumulate an adequate number of MBs to cover the microvasculature in the region of interest. These limitations are particularly restrictive in clinical applications where microvascular imaging is of diagnostic relevance (11, 16, 17) and where physiological motion is unavoidable (11, 18, 19). To improve MB localization despite high concentrations, different flavors of deep neural network architectures have been proposed (20–23). Furthermore, in (11), Huang et al. alleviated the localization problem for high-density injections by dividing the MBs into subpopulations based on flow dynamics. Unlike the polydisperse MBs commonly used in ULM, monodisperse MBs exhibit a narrow size distribution. This small size variability enables optimal tuning of the imaging frequency to match the MBs specific characteristics (e.g. MB resonance frequency), thereby enhancing acoustic performance and improving ultrasound contrast imaging. This has been demonstrated by studies showing that monodisperse MBs reduce imaging artifacts and enable the visualization of deeper blood vessels (24–26). In this study, we leverage the advantages of monodisperse MBs to overcome the trade-off between MB concentration and acquisition time. Specifically, we introduce a bi-disperse MB population composed of two distinct monodisperse MB types. We propose an uncoupling pipeline to separate these two populations based on their different frequency response. As a proof of concept, we apply this technique to ultrasound data acquired from a 3D-printed vascular phantom.

Methods

Bi-disperse MB populations

By localizing and tracking the echoes produced by individual MBs flowing in the circulation, ULM generates micro-resolved density maps (1, 4, 7, 27). In this study, we uncouple a bi-disperse MB population. The bi-disperse population is composed of two monodisperse MB populations, each having a different frequency response. In particular, we select one population ($p_{5.5MHz}$) generating mainly the fundamental response, having the resonance frequency not tuned with the transmission frequency and one population (p_{3MHz}) producing a strong nonlinear signal, having the resonance frequency matching the transmission frequency. Thus, the non-linear signal intensity allows for the uncoupling of the two populations. $p_{5.5MHz}$ and p_{3MHz} diameter and resonance frequency are presented in Table 1. Figure 1 shows the Point S Spread Function (PSF) and frequency response of $p_{5.5MHz}$ (in Figure. 1a) and p_{3MHz} (in Figure. 1b) obtained when acquiring the data at 3 MHz in water. The frequency response is evaluated as the Fourier transform along the fast time at the maximum-intensity line, shown in Figure 1 with the red dashed line. Being p_{3MHz} the population whose resonance frequency matches the transmission frequency, its frequency response is strongly nonlinear (in Figure 1b). Oppositely, $p_{5.5MHz}$'s frequency response exhibits a linear behaviour.

The bi-disperse MB population used in this study is produced by Solstice Pharmaceuticals. Each monodisperse MB population is created using a microfluidic chip device (MicroSphere Creator, Solstice Pharmaceuticals, Enschede, the Netherlands) (28). The microfluidic chip allows for control of the dimension, and consequently, the resonance frequency of the MBs, ensuring monodispersity (29). During the production phase, the chip mixes the gas and liquid with a flow rate tailored to the desired MB size. Following production, the MB size distribution and resonance frequency are measured. Figure 2 shows the size distribution of the bi-disperse population when mixed over an hour. The size distribution is measured every 5 minutes using a Coulter Counter (MultiSizer 4e, Beckman Coulter, Brea, CA). Figure 2a demonstrates that the MBs remain bi-disperse in a time window typical of ULM. Figure 2b displays the resonance frequency of $p_{5.5MHz}$

Table 1. Populations $p_{5.5MHz}$ and p_{3MHz} dimensions in micro-meter and resonance frequency in MHz.

	$p_{5.5MHz}$	p_{3MHz}
Diameter	2.5 μm	4.0 μm
Resonance Frequency	5.5 MHz	3 MHz

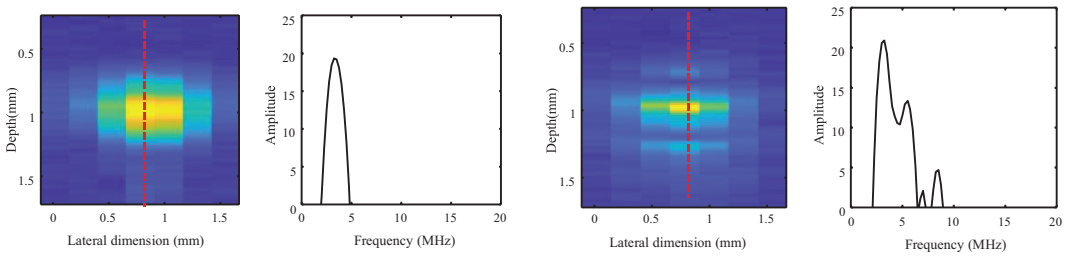

Figure 1. Full field Point Spread Function (PSF) and frequency response in dB for $p_{5.5MHz}$ (a) and p_{3MHz} (b). The frequency response is evaluated as the Fourier transform along the fast time at the maximum-intensity line, highlighted by the red dashed line.

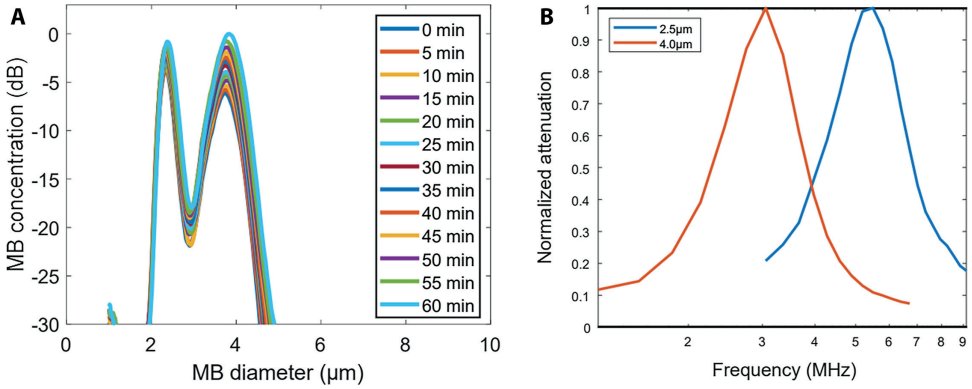

Figure 2. Size distribution (a) and resonance frequency (b) measurements for $p_{5.5MHz}$ (2.5 μm) and p_{3MHz} (4.0 μm), evaluated after MB production.

and p_{3MHz}. As in (30), the resonance frequency is estimated through attenuation for individual populations. Briefly, a 7.5 MHz (for $p_{5.5MHz}$) and 5 MHz (for p_{3MHz}) transducer (V309-SU and V320-SU, Olympus, Waltham, Massachusetts, USA) generate an acoustic beam, which after traversing a bubble screen, is reflected and received by the same transducer. The pulser (DPR300 Ultrasonic Pulser Receiver JSR Ultrasonic NY, USA) synchronises the transmitting and receiving phases (30). In transmission, a broad-bandwidth pulse is sent to the bubble screen. Then, the attenuation is measured as the difference between the received power spectrum crossing the MB screen and a reference spectrum measured without MBs. Finally, the resonance frequency is estimated to be the frequency showing the highest attenuation. The high control of the MB dimensions and their stability over time offers the possibility to select two distinguishable MB populations.

Data acquisition

Ultrasound data were acquired with MBs flowing through a custom 3D printed flow phantom running at a constant flow rate with MBs varying concentrations (dilution of 10000x-20000x in de-gassed water). The phantom is printed in collaboration with PROM Facility, Rovereto, Italy, using the Selective Sintering Laser technique, which fuses polymer powders material via laser (31). The laser thermal source allows heating of the polymer at a specific location, thus building the 3D solid structure layer-bylayer at a sub-millimetre scale. The material used to print the 3D vascular phantom (Flexa TPU, elastic module 76 MPa, and, density 1.04 g/cm^2) permitted ultrasound imaging. The 3D model design is visible in Figure 3. The model has three injection points, and channels with varying dimensions ranging from a diameter of 2 mm to 1.5 mm. The experimental data acquisition is

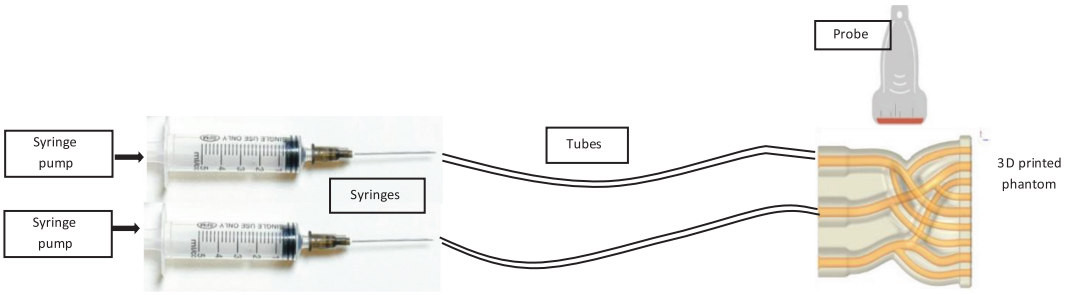

Figure 3. Experimental set up. The phantom has three injection points, two of which are connected through tubes to a pair of syringes, each containing a specific MB population. Continuous injections are performed using a syringe pump. Data acquisitions are performed using the ULAOP and and a linear array.

performed with the phantom positioned vertically in a tissue-mimicking gel to avoid any movement during the acquisition process, as shown in Figure 3. In the study, we utilize two injection points, each connected to a syringe pump flowing at a constant rate of 2 ml/min. Each syringe contains a different MB population. MB populations are diluted in de-gassed water and kept in suspension with a steering plate. Injections of 20 ml are performed continuously. Ultrasound data are acquired for each MB population singularly and simultaneously. For individual injections, we inject MBs into the first channel and water in the second channel for $p_{5.5MHz}$, while for p_{3MHz}, the injections are reversed.

To acquire the radio-frequency data, we employ a programmable ultrasound platform (ULAOP), and a linear array probe (Esaote LA533, Florence, Italy (32)), placed horizontally to the 3D printed channels, as shown in Figure 3. Line-by-line was implemented acquiring 64 lines for each image. A pulse with a center frequency of 3 MHz and bandwidth of 1 MHz was used in transmission. For each record, 250 frames are acquired with a frame rate of 187 Hz. The sampling frequency is 50 MHz.

ULM data processing

To generate the density and dynamic maps of the MB populations, we implement a common ULM framework, summarized in Figure 4. After data acquisition, filtering is applied to the ultrasound RF data. Specifically, filtering is implemented by a Butterworth band-pass filter, with 2 MHz and 20 MHz as lower and upper cut-off frequencies. A singular value decomposition (SVD) filter is then applied. The SVD filter removes the first k-value of the decomposition, assuming that these represent the coherent spatio-temporal background signal (1, 4). In this study, the k-value is experimentally selected to 5, consistent with the range discussed in other studies (4, 33). Next, the MBs uncoupling is deployed to generate two subsets of ultrasound images, each of which represents one of the uncoupled populations (h_{p3MHz} for population p_{3MHz} and $h_{p5.5MHz}$ for population $p_{5.5MHz}$). Finally, the ULM framework comprising detection, localization, tracking, and accumulation is applied. The detection step is performed using two different methods (I_{pix} and ncc):

1. Localization using Pixel Intensity (I_{pix}). The technique, presented by Couture et. al. (33), assumes that an MB echo is represented by the brightest pixels in the ultrasound image. The technique requires estimating m (the number of MBs) present in each frame. Here, m is optimally selected to 30-50 MBs/frame based on the dilution. Next, the m brightest pixels, isolated at least by the dimensions of a MB PSF are considered MB detections.
2. Localization through correlation (ncc). Similar to (5, 33), this technique utilizes a mean PSF obtained by acquiring the ultrasound data of $p_{5.5MHz}$ and p_{3MHz} in water. The PSF is specific to each population and is obtained by averaging the PSF of 20 MBs in different acquisitions. The PSF for the two populations can be

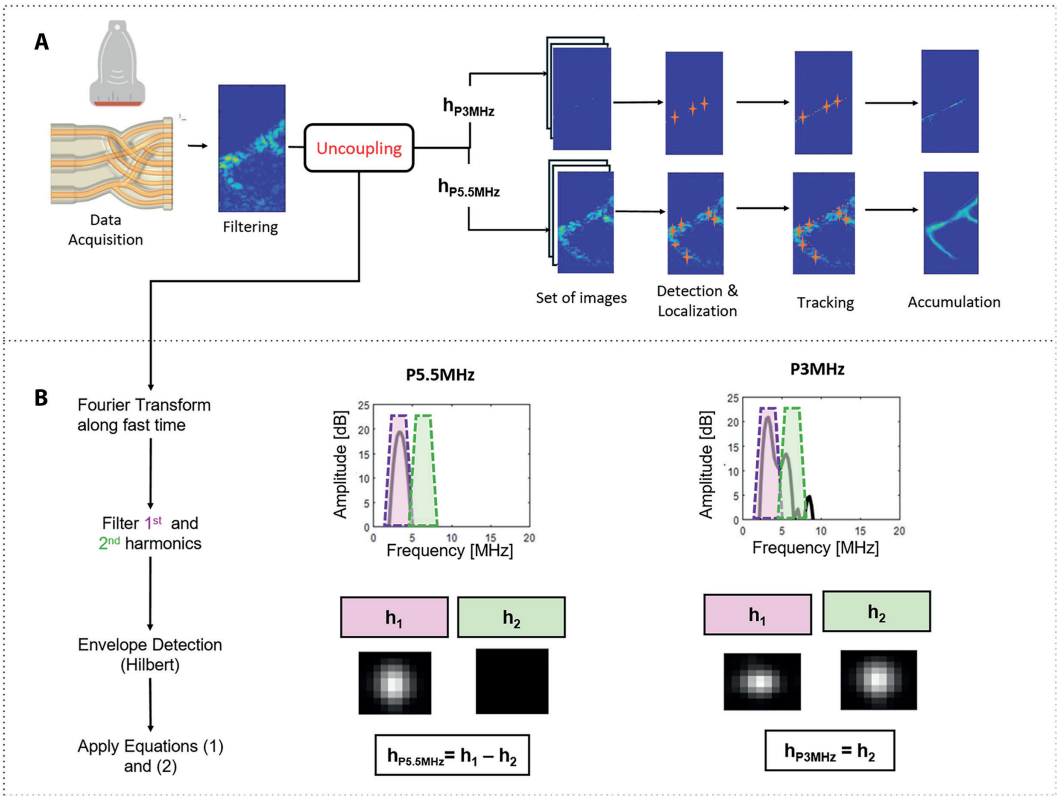

Figure 4. At the top (a) uncoupling pipeline for the bi-disperse MB population. Uncoupling is performed after data acquisition and filtering. As a result of the uncoupling, a set of images for each population ($hp_{5.5MHz}$ for $p_{5.5MHz}$ and hp_{3MHz} for p_{3MHz}) are obtained. Next, a ULM framework comprising of detection, localization, tracking and accumulation, is applied. At the bottom (b) detail of the uncoupling procedure of $p_{5.5MHz}$ and p_{3MHz}. First, the first and second harmonics are filtered employing a Butterworth filter in the frequency domain. Successively, the envelope detection is used to generate the images of the first (h_1) and second harmonics (h_2). Images of the two populations $hp_{5.5MHz}$ and hp_{3MHz} are evaluated as $h_1 - h_2$ and h_2 respectively.

seen on the right side of Figure 4b. For each frame, a 2D normalized cross-correlation between the filtered images and the MB PSF is evaluated. This results in a crosscorrelation map, where the peaks correspond to MB detections. To further improve the detection performance, a threshold of 0.5 is selected as the minimum correlation to consider the pixels as MB signals. This threshold value was empirically selected based on the data of this study. If the correlation is lower than the threshold value, the pixels are considered background noise and are excluded.

3. Localization through correlation and pixel intensity (I_{pix} + *ncc*). This detection technique consists of merging in cascade the *ncc* and I_{pix} methods. In particular, the detections identified by *ncc* proceed to the localization step only if their intensity, evaluated at its center, is among the *k* brightest pixels. The correlation threshold and *k* are optimally selected as 0.4 and 12 respectively.

The comparison between these detection algorithms provides proof of the robustness of the proposed uncoupling pipeline. In this way, we confirm the uncoupling capability when using a standard algorithm (brightest pixel) while demonstrating the possibility of improving performance using a model-based algorithm (normalized-cross-correlation) and

a combination of the two. To ensure a fair comparison between the methods, the parameter values are empirically determined through a parameter search optimization. Note that the results using I_{pix} + *ncc* detection method are produced only for simultaneous MB injections as this represents the more realistic scenario. After detection, a Gaussian fitting (4, 7, 1) is performed to further refine the localization estimate. For each detection, a Gaussian distribution is fitted by subsampling the pixels by a factor of 10, as described in (1). Next, MB centroids for each population are tracked through a bipartite matching algorithm. The algorithm finds the optimal frame-to-frame pair for all the MB signals, matching them in such a way that the total distances of all the MBs are minimized (1, 32, 34). Repeating the process for all the frames in a record generates MB tracks. To improve tracking precision, MBs with persistence shorter than 7 frames are discarded. Finally, density and dynamic maps are obtained through the accumulation of these tracks.

Microbubble uncoupling

The uncoupling is performed as a pre-processing stage (see Figure 4). First, we apply a Butterworth filter to separate the first and second harmonic components. The filter has a center frequency of 3 MHz and 6 MHz for the first and second harmonic respectively, and 1 MHz of bandwidth. Next, we apply a Hilbert transform to generate the ultrasound images associated with the first (h_1) and second (h_2) harmonic signal. As shown by Figure 4b, the uncoupling is performed as follows:

- $p_{5.5MHz}$ is the population characterized by a resonance frequency (5.5 MHz) not matching the transmission frequency (3 MHz) and, as a consequence, by a linear response. $p_{5.5MHz}$ images ($h_{p5.5MHz}$) are obtained by subtracting the first (h_1) and second (h_2) harmonic images:

$$h_{p5.5MHz} = h_1 - h_2. \quad (1)$$

An example of PSF for h_1, h_2 and $h_{p5.5MHz}$ is shown in Figure 5b.

- p_{3MHz} is the population whose resonance frequency matches the transmission frequency (3 MHz) and thus has a strong nonlinear

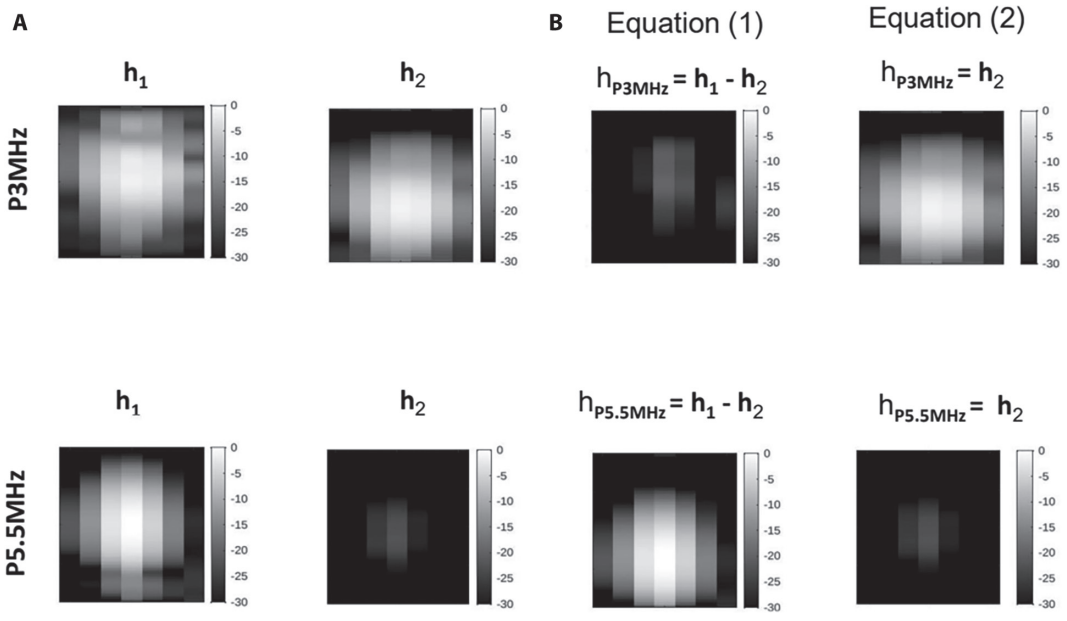

Figure 5. Example of h_1 and h_2 for populations p_{3MHz} and $p_{5.5MHz}$ (a). Results of applying Equations 1 and 2 to both populations(b).

response. p_{3MHz} is isolated by imaging the second harmonic:

$$h_{p3MHz} = h_2. \quad (2)$$

The first (h_1) and second (h_2) harmonic PSFs of a MB belonging to population p_{3MHz} are shown in Figure 5b.

Note that, by applying 1 to population p_{3MHz} would cancel out this MB population signal. Similarly, using equation 2 to image $p_{5.5MHz}$ would cancel out its contribution. As such, the equations allow to selectively image each MB population, thus permitting the uncoupling. To verify this, we perform the experiments having only one population injected in one channel, meanwhile flushing water in the other. This choice would allow us to understand the potential cross-talk between the two MB populations. Next, we apply the proposed pipeline when injecting the two MB populations at the same time.

Results

This work demonstrates the feasibility of uncoupling the bi-disperse MB population based on the intensity of each MB's population nonlinear response. In fact, we are able to reconstruct density and flow dynamics maps in a 3D printed phantom using the proposed uncoupling pipeline (Figure 4). Figures 6a and 6b show respectively the density and flow direction maps for the detection method based on the brightest pixels (I_{pix}) and normalized cross-correlation method (*ncc*). Data are acquired after separate injections of each population, and the uncoupling generates images of population $p_{5.5MHz}$ and p_{3MHz}, marked as $h_{p5.5MHz}$ and h_{p3MHz}. Figure 6b shows the flow direction images which are color-coded, with red marking the flow away from the probe, and blue the flow towards the probe. Individual injections serve as an initial validation for the uncoupling pipeline while having a ground truth. During single injections and in case of perfect uncoupling, the residual images obtained by attempting to image the non-injected population should be empty. For instance, in 6a first column, only p_{3MHz} has been injected. After injection, the uncoupling and ULM pipeline produce images of both populations h_{p3MHz} and $h_{p5.5MHz}$, using Equations 1 and 2, respectively. As such, h_{p3MHz} displays tracks of the MB population, since p_{3MHz} is the population injected. On the other hand, $h_{5.5MHz}$ is empty, as it attempts to image the population which is not present. We mark the residual images with a red background for both the density and flow direction maps (Figure 6). Intensity profiles of two cross-sections for both detection methods (I_{pix} and *ncc*) are displayed in Figure 7a and 7b, for p_{3MHz} and $p_{5.5MHz}$ respectively. Additionally, the full width half maximum (FWHM) values further highlight the ability of the proposed pipeline to depict the geometry of the vascular structures (see arrows in Figure 7).

Table 2 shows the quantitative metrics for the density maps generated for the two populations utilizing I_{pix} and *ncc* as detection methods. The table presents the results in terms of saturation, evaluated as the number of pixels covered by MBs tracks, mean detections per frame and mean tracks per record. The mean track/record is the average value of the total tracks found after applying the bi-partite tracking algorithm. The mean detections/frame and mean tracks/frame metrics are particularly relevant in discussing the performance of the uncoupling pipeline. In fact, knowing which MB population is present in each channel, the number of residual detections and tracks is a direct evaluation of false positives. Finally, we evaluate the percentage of mean accepted track per record, which represents the percentage of the total number of tracks after filtering out short tracks. This metric reflects tracks quality, since short tracks are likely the results of poor detections and noise, and, as such, are unreliable for micro-vascular reconstruction (8, 35). Figure 8 shows the *ncc* generated tracks for both populations superimposed with the 3D printed phantom design. Figure 9 and Table 3 show the density maps and the evaluation metrics generated when injecting the two populations simultaneously for the three detection methods. Furthermore, a comparison with density maps generated by using a standard ULM pipeline before uncoupling for I_{pix} and *ncc* detection methods is presented in Figure 10. Note that for I_{pix} detection method the number of MBs present per frame has been increased to account for more MBs in one frame. Regarding the *ncc* detection method, the same correlation threshold has been applied.

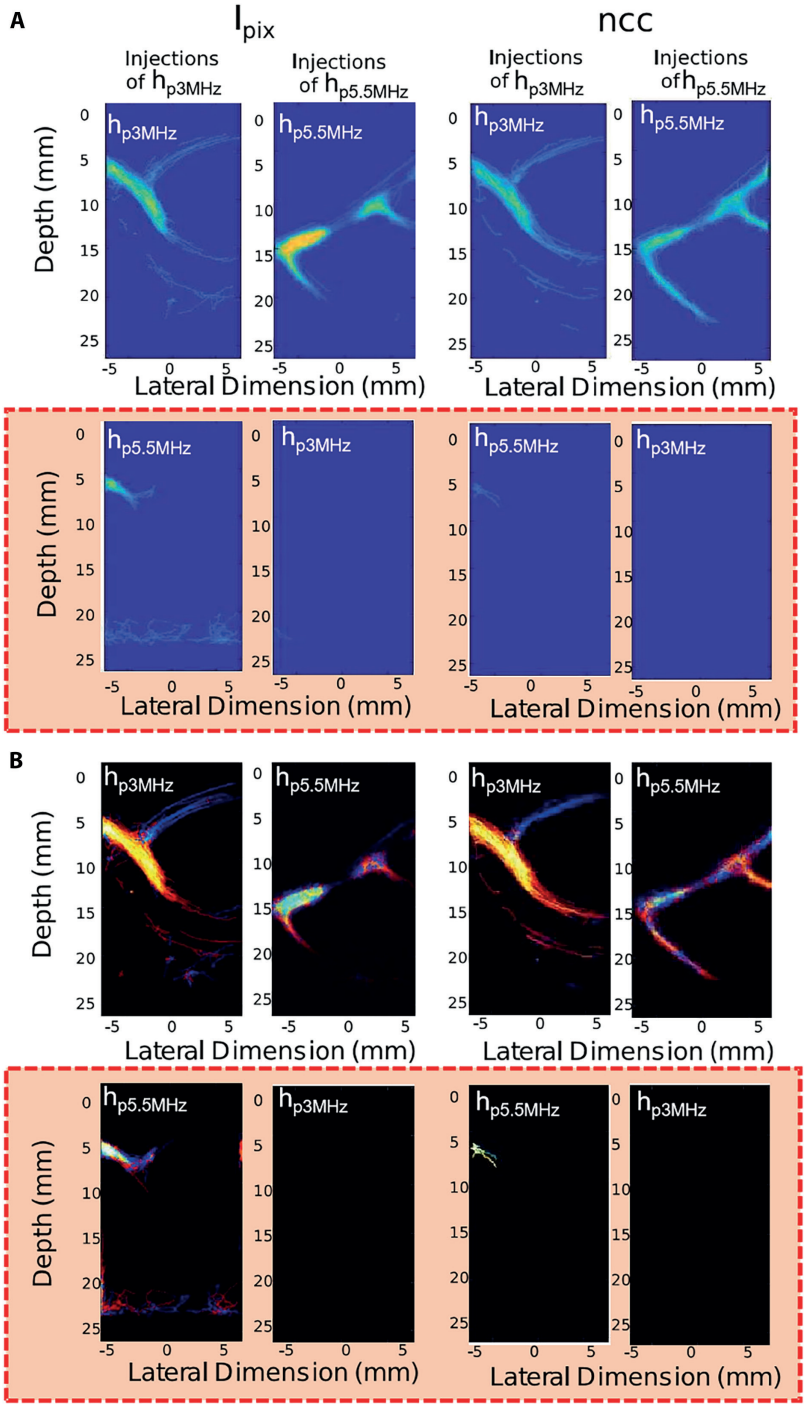

Figure 6. ULM-generated density (a) and flow direction (b) maps for population p_{3MHz} (h_{p3MHz}) and $p_{5.5MHz}$ ($h_{p5.5MHz}$) after individual injection as indicated by each column subtitle. The first row of (a) and (b) represents the images of p_{3MHz} and $p_{5.5MHz}$ when injecting MBs; the second row shows the images of each when injecting the other. Images are shown for detection methods I_{pix} and ncc. In (b), flow direction is color-coded: red = flow away from the probe, blue = flow toward the probe.

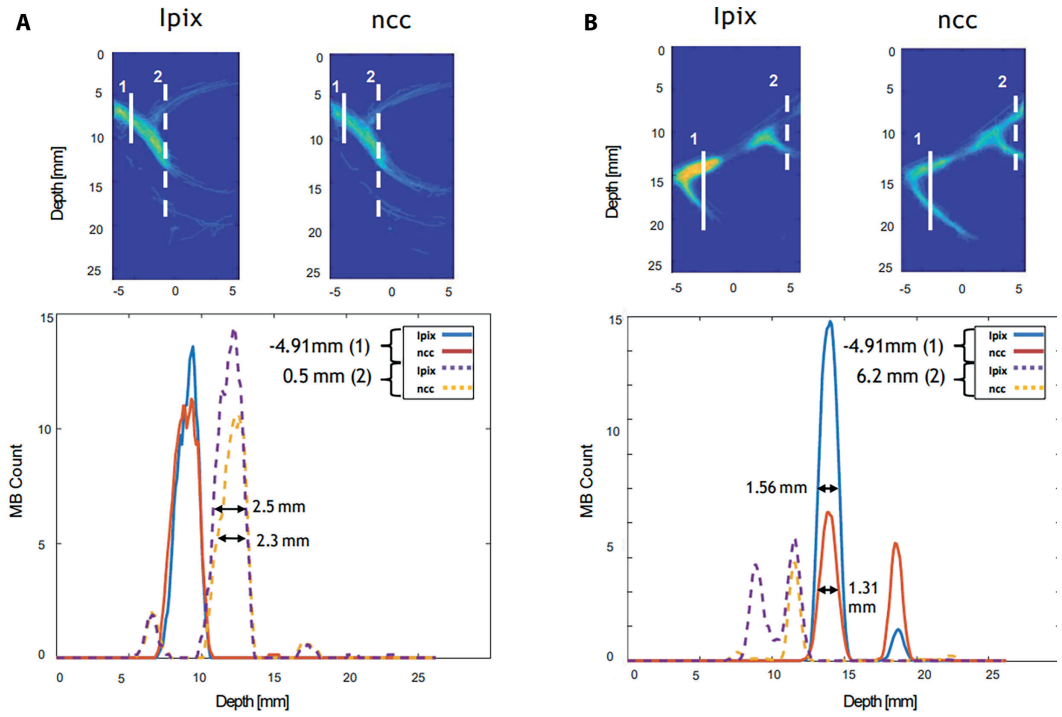

Figure 7. One-dimensional intensity profiles at different depths as indicated in the top images corresponding to the solid (1) and dashed line (2). The FWHM values are indicated in millimeters and by black arrows. Images are shown for detection methods I_{pix} and ncc, for population p_{3MHz} (a) and population $p_{5.5MHz}$ (b).

Table 2. Results for the two detection methods I_{pix} (brightest pixel) and ncc (normalized cross-correlation).

	Ipix			
	Injections of p_{3MHz}		**Injections of $p_{5.5MHz}$**	
	h_{p3MHz}	$h_{p5.5MHz}$	$h_{p5.5MHz}$	h_{p3MHz}
Saturation (%)	9.1	4.1	10	0.5
Mean detections/frame	6	4.2	15	2
Mean tracks/record	150.3	124.9	358	20
Mean accepted tracks (%)	57	15	27.7	1
	ncc			
	Injections of p_{3MHz}		**Injections of $p_{5.5MHz}$**	
	h_{p3MHz}	$h_{p5.5MHz}$	$h_{p5.5MHz}$	h_{p3MHz}
Saturation (%)	10.7	1	12	0.4
Mean detections/frame	5	1.5	11.2	1
Mean tracks/record	104.5	14	334	12
Mean accepted tracks (%)	28.2	3.1	16.7	0.1

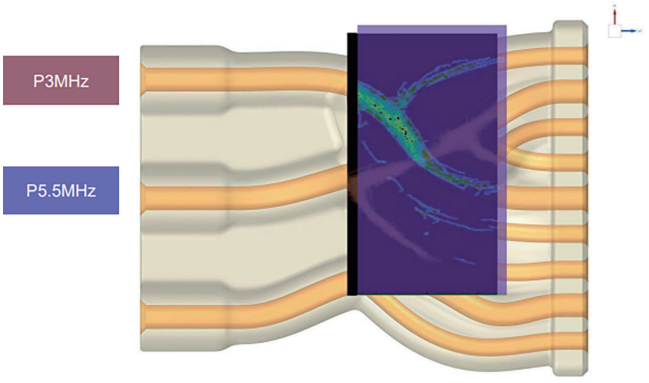

Figure 8. Superimposed image of the ULM generated density maps with the phantom design utilizing ncc as detection method.

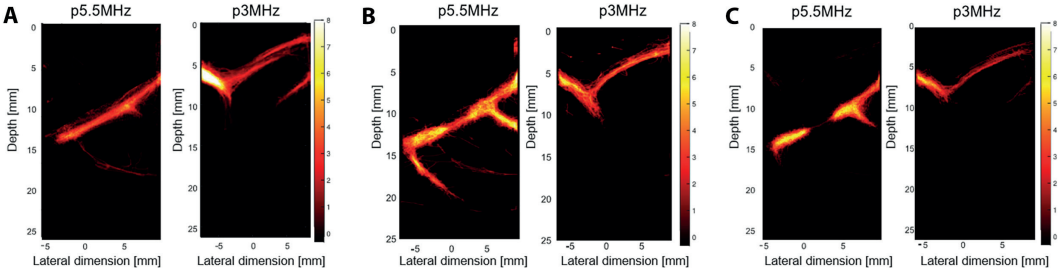

Figure 9. Density maps generated after uncoupling when injecting the MB populations simultaneously. Maps are generated using Ipix (a), ncc (b) and Ipix+ncc (c).

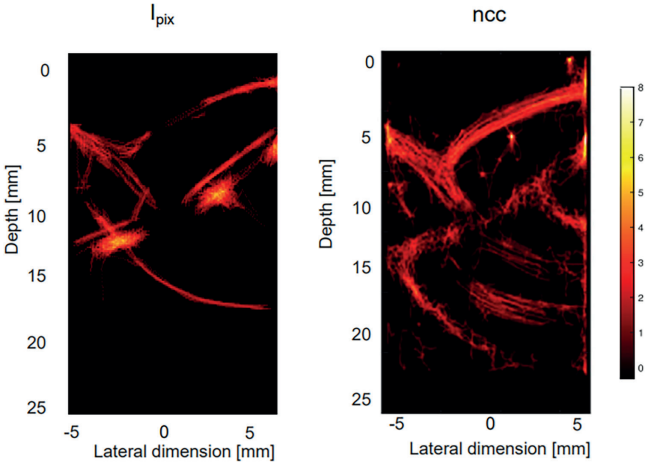

Figure 10. Standard ULM generated density maps (before uncoupling) for the simultaneous injections using two detection methods: I_{pix} and ncc.

Table 3. Results for the three detection methods when injecting the two MB populations simultanously.

	I_{pix}		*ncc*		I_{pix} + *ncc*	
	$h_{p5.5MHz}$	h_{p3MHz}	$h_{p5.5MHz}$	h_{p3MHz}	$h_{p5.5MHz}$	h_{p3MHz}
Saturation (%)	**14.1**	**12.4**	**13.2**	**18.3**	**13.1**	**8.9**
Mean detections/frame	**10**	**10**	**21**	**17**	**12**	**12**
Mean tracks/record	**168.6**	**347**	**822**	**923**	**199**	**84**
Mean accepted tracks (%)	**74.2**	**44.7**	**57.3**	**62.8**	**72.2**	**82.5**

Discussion

In this article, we present an acoustically separable bi-disperse MB population composed of two monodisperse MB populations. Separation is achieved through an uncoupling pipeline that exploits differences in the nonlinear acoustic responses of the two MB populations. This approach potentially enables the use of higher MB concentrations in ULM vascular imaging, resulting in faster vascular filling and shorter data acquisition times. Reducing acquisition times is essential for clinical translation of ULM, as it decreases susceptibility to physiological motion such as respiration, cardiac pulsatility, and organ displacement. Results highlight the performance of the technique when individual (Figure 6) and simultaneous (Figure 9) injections are performed. Figures 6 and 9 show density maps obtained utilizing different detection methods: the brightest pixel (I_{pix}), a context-unaware detection method, and normalized cross-correlation (*ncc*), a model-based detection approach and the combination of the two (I_{pix} + *ncc*) (only for simultaneous injections). These results confirm the robustness of the proposed uncoupling pipeline in separating the bi-disperse population. Furthermore, the flow direction maps (Figure 6b) demonstrate that the proposed pipeline preserves flow information. Note how the color encoding, with blue representing MB flow towards the probe and red away from it, is consistent with the direction imposed by the experimental setup. The performance of the proposed method is further supported by the quantitative results in Table 2, where saturation, mean detections and mean tracks decrease in the residual column (marked in red in Table 2, reinforcing uncoupling capability). Figure 6 demonstrate that *ncc* outperforms I_{pix}. This is visible from the spurious tracks present in the residual images. For instance, observe the tracks present in the lower part of image $h_{p5.5MHz}$ generated using I_{pix} for injections of p_{3MHz}. In this image, I_{pix}-generated images show a high number of false positives tracks compared to *ncc*. The reason for I_{pix} lower uncoupling performance lies in the way I_{pix} works. I_{pix} detections are pushed to find the m brightest pixels. However, these pixels might be the result of uncoupling errors or the filtering results, leading to false positive detections and the appearance of spurious tracks. I_{pix} detects on average 4.2 MBs/frame for $p_{5.5MHz}$ when injecting p_{3MHz} (see Table 2). For the same case, *ncc* detects 1.5 MBs/frame, showing better uncoupling performance. The improved separation capability of a model-based detection method (*ncc*) is confirmed by the mean tracks per record and the mean percentage of accepted tracks in Table 2. On average for p_{3MHz} injections, *ncc* accepts 3.1 % of the detected tracks for $p_{5.5MHz}$, whereas I_{pix} accepts 15 % of the tracks, causing the appearance of false tracks. Despite a similar mean number of tracks/record for p_{3MHz} for acquisitions where only p_{3MHz} is present, the mean tracks/record substantially drops for $p_{5.5MHz}$ (from 124.9 to 14 tracks/record) when using *ncc* method. The high number of tracks indicates a large number of tracks likely caused by false positive MB detections, reflecting I_{pix} poorer uncoupling performance. However, these false positive tracks are partially filtered out by the track length threshold. The robustness of *ncc*'s detection performance is further evident from the density profiles shown in Figure 7. For instance, observe the profile for cross-section 1 in Figure 7b, where *ncc* allows the visualization of different phantom branches with comparable intensity. Although I_{pix} produces tracks for both channels, the number of detected MBs flowing in one of the two channels is significantly

higher. While *ncc* shows better separability, the performance improvement comes at the cost of a higher computational demand. Table 3 confirms the superiority of *ncc* for uncoupling the two populations when injected together across all the metrics. The mean detections per frame (see Table 3) are higher for the *ncc* method, leading to more tracks and a more saturated final density map, confirming the analysis of single injections. However, the tracks obtained with the *ncc* method for population p_{3MHz} (Figure 9 b) appear to be more scattered and less smooth, probably due to the higher number of detections, which makes tracking more challenging. Figure 9a and b present a few spurious tracks, which are absent for the results produced by the I_{pix} + *ncc* method (Figure 9c). In fact, the number of discarded tracks, observable by the higher number of accepted tracks in Table 3, is lower with respect to the other two methods. This can be explained by the fact that I_{pix} + *ncc* method acts as a two layer filter, one based on correlation and the other based on pixel intensity, which selects few and more likely MBs detections. It is worth noting that this method requires fine-tuning of more parameters; k' the number of brightest pixels and the correlation level. Increasing k' means more MBs detected, which could be noise. However, if the correlation threshold is set high enough (e.g. > 0), the possibility of these detections being noise is low. Although the approach I_{pix} +*ncc* produces similar results to *ncc*, the need of more data for vascular filling and the need of further parameter tuning, makes it more difficult to translate clinically. Besides the detection method, the number of tracks resulting from the uncoupling allows to discriminate the two populations. To demonstrate the potential advantage of using the proposed technique with respect to standard ULM, we compare the density maps generated before (Figure 10) and after uncoupling (Figure 9). Compared to standard ULM, the reconstructed maps highlight how the proposed pipeline better reconstructs the geometry of the phantom for both methods. The main reason for the improved performance can be explained by the fact that, when both MBs are present, there is a higher concentration of MBs, which make standard ULM more difficult. For I_{pix} density maps, fewer tracks are present, probably due to the higher number of overlapping MBs detections. On the other hand, *ncc* appears to reconstruct the vasculature, but more spurious tracks are present. These results strengthen the clinical utility of the proposed uncoupling pipeline, which improves the MB localization efficacy and imaging speed of ULM under high MB concentrations. All of this might alleviate the long acquisition times hindering ULM practical implementation. From a clinical standpoint, reduced acquisition times are especially important in applications in which microvascular characterization yields clinically meaningful biomarkers and motion remains a major challenge. For example, in oncologic imaging, characterization of tumor microvascular density, tortuosity and flow provides clinically meaningful biomarkers, but prolonged acquisition times increase sensitivity to motion artifacts (11, 18). Similarly, in renal imaging where respiratory motion is prominent, the feasibility of ULM is strongly influenced by acquisition duration (19, 20). In these contexts, the ability to operate at higher MB concentrations, while preserving separability may improve robustness to motion and support the translation of ULM into routine clinical practice. Results highlight the advantage of using 3D printed vascular phantoms as physical ground truth for assessing ULM-generated maps. There are few missing branches in the reconstructed density maps, which can be explained by the misalignment between the imaging plane and the phantom positioning. Nevertheless, the reconstructed tracks align with the phantom geometry (Figure 8) and the vascular dimension estimated from ULM images are consistent with those of the phantom. In Figure 7, the channel width is evaluated at the FWHM of the intensity profiles and found to be approximately 2 mm, matching the phantom's inner diameter. This study presents several limitations. Firstly, the stability and separability studies have been tested on data acquired in a 3D printed phantom. While these *in vitro* results provide an opportunity to validate the proposed approach, testing it on clinical *in vivo* data is essential to assess the method's feasibility in a physiological context, characterized by many challenges, such as tissue attenuation, clutter noise, spectral distortion and motion. Furthermore, a natural extension of the study involves injecting a mixture of the two monodisperse populations, rather than performing injections either individually or simultaneously. This next step is crucial

not only for validating the MB response when both populations are present, but also verifying the uncoupling performance of the proposed algorithms and investigating the feasibility of increasing MB concentrations. By mixing the two populations, we can assess the effectiveness of the uncoupling technique in real-world scenarios. Furthermore, given the control on 64 elements, line-by-line imaging has been implemented for this study. While this choice guarantees a wide field of view, it comes at the price of lower frame rates compared to ultrafast imaging normally implemented in standard ULM. In future *in vivo* studies, we plan to implement plane wave imaging, which would allow to achieve higher frame rates. Finally, a limitation of this study is the variability of the *in vitro* experiments due to the manual selection of the imaging plane and phantom instability. As a consequence, some vascular branches present in the phantom are not visible in the final density and velocity maps. To solve this, improvements on the replicability of the set up can be performed. In addition, 3D imaging would solve the imaging plane selection issue.

Conclusions

In this study, we demonstrate the feasibility of uncoupling a bi-disperse MB population. Results show the ability of the proposed uncoupling pipeline to generate dynamic and functional maps when singularly and simultaneously injecting distinct MB populations in two separate phantom branches. We tested the proposed uncoupling framework using two detection methods. I_{pix} performs detection based on the brightest pixels, whereas *ncc* utilizes cross-correlation for detecting MBs. Both methods allow the uncoupling of the two selected populations. However, results show a better performance of a model-based approach (*ncc*) with respect to a context-unaware method (I_{pix}). Furthermore, we compare the reconstructed density maps before and after uncoupling. Results confirm that standard ULM fails to capture the vasculature, possibly due to high MBs concentrations, whereas by utilizing the uncoupling technique, the reconstructed vascular structures appear to better represent the ground truth geometries. Results confirm that standard ULM fails to capture the vasculature, possibly due to high MBs concentrations, whereas by utilizing the uncoupling technique, the reconstructed vascular structures appear to better represent the ground truth geometries. The results demonstrate that the proposed approach can address ULM's key challenges, including prolonged acquisition times and low MB concentrations, thereby supporting its practical and clinical applicability. As a future work, we plan to simultaneously inject in the same channel the two populations to verify the advantage of using a bi-disperse population over a poly- and/or mono-disperse population. Furthermore, we plan to perform *in vivo* experiments to verify the separability of the bi-disperse MB population and the performance of the proposed uncoupling pipeline towards advanced ULM. This would ultimately allow for an increase of MBs concentrations, thus alleviating the need for long acquisition time for micro-vascular imaging. In addition, it is worth highlighting that in this study we 3D-printed a vascular phantom compatible with ultrasound imaging. As a next step, we aim at 3D printing structures having dimensions and geometries comparable with the *in-vivo* vascular bed. The phantoms would provide a fully controllable tool to validate ULM's results both in terms of geometry depiction and velocity information. Finally, the use of different populations might benefit not only on a practical level (shortening the acquisition time) but also on a more diagnostic and monitoring level. Distinguishable populations might represent a first step towards an advanced and optimized contrast-enhanced ultrasound imaging system. For instance, depending on the MBs' sizes, different populations might selectively transit in micro-vessels characterized by different properties, expanding ULM capability to characterize the microvascular flow.

Supplementary information. See supplementary material for images and videos pre- and post- uncoupling on the website: https://www.mattioli1885journals.com/index.php/theultrasoundjournal/article/view/18060

Acknowledgements: Part of this work was supported by the Hub Life ScienceAdvanced Diagnosis (HLS-AD), PNRR PNC-E3-2022-23683266 PNC-HLS-DA, INNOVA – CUP: E63C22003780001, funded by the Italian Ministry of Health

under the National Complementary Plan Innovative Health Ecosystem - Unique Investment Code: PNC-E.3. We thank PROM Facility, in Rovereto, Italy for the support in the 3D printing of the vascular phantom. In particular, M. Perini and C. Malacarne for 3D designing, material selection and printing of the vascular phantom.

Author's contributions: GT, LTW, CB, WVH, LD contributed to the study design and development. GT performed data acquisition and analysis. LTW, CB, WVH contributed to microbubble production. GT, WVH, LD contributed to writing the manuscript and revisions of the study. All authors read and approved the final manuscript.

Availability of data and material: The data that supports the findings of this study are available from the corresponding author upon reasonable request

Ethics approval and consent to participate: No patient is part of this work.

Competing interests: The authors have no relevant financial or non-financial interests to disclose. The authors have no conflicts of interest to declare that are relevant to the content of this article.

Declaration on the use of AI: none.

References

1. Heiles B, Chavignon A, Hingot V, Lopez P, Teston E, Couture O. Performance benchmarking of microbubble-localization algorithms for ultrasound localization microscopy. Nat Biomed Eng. 2022 May;6(5):605-616. doi: 10.1038/s41551-021-00824-8.
2. Song P, Rubin JM, Lowerison MR. Super-resolution ultrasound microvascular imaging: Is it ready for clinical use? Z Med Phys. 2023 Aug;33(3):309-323. doi: 10.1016/j.zemedi.2023.04.001.
3. Carovac A, Smajlovic F, Junuzovic D. Application of ultrasound in medicine. Acta Inform Med. 2011 Sep;19(3):168-71. doi: 10.5455/aim.2011.19.168-171.
4. Couture O, Besson B, Montaldo G, Fink M, Tanter M. Microbubble ultrasound super-localization imaging (MUSLI). 2011 IEEE International Ultrasonics Symposium. 2011 Oct;1285–7.
5. Christensen-Jeffries K, et al. Super-resolution Ultrasound Imaging. Ultrasound Med Biol. 2020 Apr;46(4):865-891. doi: 10.1016/j.ultrasmedbio.2019.11.013.
6. Siepmann M, Schmitz G, Bzyl J, Palmowski M, Kiessling F. Imaging tumor vascularity by tracing single microbubbles. 2011 IEEE International Ultrasonics Symposium. 2011 Oct;1906–9.
7. Dencks S, Schmitz G. Ultrasound localization microscopy. Z Med Phys. 2023 Aug;33(3):292-308. doi: 10.1016/j.zemedi.2023.02.004.
8. Dollet B, van der Meer SM, Garbin V, de Jong N, Lohse D, Versluis M. Nonspherical oscillations of ultrasound contrast agent microbubbles. Ultrasound Med Biol. 2008 Sep;34(9):1465-73. doi: 10.1016/j.ultrasmedbio.2008.01.020.
9. Desailly Y, Pierre J, Couture O, Tanter M. Resolution limits of ultrafast ultrasound localization microscopy. Phys Med Biol. 2015 Nov 21;60(22):8723-40. doi: 10.1088/0031-9155/60/22/8723.
10. Huang C, et al. Short Acquisition Time Super-Resolution Ultrasound Microvessel Imaging via Microbubble Separation. Sci Rep. 2020 Apr 7;10(1):6007. doi: 10.1038/s41598-020-62898-9.
11. Tang S, et al. Kalman Filter-Based Microbubble Tracking for Robust Super-Resolution Ultrasound Microvessel Imaging. IEEE Trans Ultrason Ferroelectr Freq Control. 2020 Sep;67(9):1738-1751. doi: 10.1109/TUFFC.2020.2984384.
12. Errico C, Pierre J, Pezet S, Desailly Y, Lenkei Z, Couture O, Tanter M. Ultrafast ultrasound localization microscopy for deep super-resolution vascular imaging. Nature. 2015 Nov 26;527(7579):499-502. doi: 10.1038/nature16066.
13. Deffieux T, Demene C, Pernot M, Tanter M. Functional ultrasound neuroimaging: a review of the preclinical and clinical state of the art. Current Opinion in Neurobiology. 2018 Jun;50:128-135. DOI: 10.1016/j.conb.2018.02.001.
14. Lin F, Shelton SE, Espíndola D, Rojas JD, Pinton G, Dayton PA. 3-D Ultrasound Localization Microscopy for Identifying Microvascular Morphology Features of Tumor Angiogenesis at a Resolution Beyond the Diffraction Limit of Conventional Ultrasound. Theranostics. 2017 Jan 1;7(1):196-204. doi: 10.7150/thno.16899.
15. Li T, Sun H, Gai Y, Zhu L, Yang J, Ma C. Ultrasound Localization Microscopy for the Assessment of Microvascular Abnormalities in Transplant Renal Artery Stenosis. Ultrasound Med Biol. 2025 Nov;51(11):2120-2124. doi: 10.1016/j.ultrasmedbio.2025.07.032.
16. Hu X et al. Microvascular heterogeneity exploration in core and invasive zones of orthotopic rat glioblastoma via ultrasound localization microscopy. Eur Radiol Exp. 2025 Mar 5;9(1):30. doi: 10.1186/s41747-025-00555-4.
17. Josquin Foiret, Zhang H, Tali Ilovitsh, Mahakian LM, Tam S, Ferrara KW. Ultrasound localization microscopy to image and assess microvasculature in a rat kidney. Scientific Reports. 2017 Oct 20;7(1).
18. Hingot V, Errico C, Heiles B, Rahal L, Tanter M, Couture O. Microvascular flow dictates the compromise between spatial

resolution and acquisition time in Ultrasound Localization Microscopy. Sci Rep. 2019 Feb 21;9(1):2456. doi: 10.1038/s41598-018-38349-x.
19. Li Y, Huang L, Zhang J, Huang C, Chen S, Luo J. Localization of High-concentration Microbubbles for Ultrasound Localization Microscopy by Self-Supervised Deep Learning. 2021 Sep 11;1–4.
20. Shin Y, et al. Context-aware deep learning enables high-efficacy localization of high concentration microbubbles for super-resolution ultrasound localization microscopy. Nat Commun. 2024 Apr 4;15(1):2932. doi: 10.1038/s41467-024-47154-2.
21. van Sloun RJG, et al. Super-Resolution Ultrasound Localization Microscopy Through Deep Learning. IEEE Trans Med Imaging. 2021 Mar;40(3):829-839. doi: 10.1109/TMI.2020.3037790.
22. Lerendegui M, et al. ULTRA-SR Challenge: Assessment of Ultrasound Localization and TRacking Algorithms for Super-Resolution Imaging. IEEE Trans Med Imaging. 2024 Aug;43(8):2970-2987. doi: 10.1109/TMI.2024.3388048.
23. Helbert A, Gaud E, Segers T, Botteron C, Frinking P, Jeannot V. Monodisperse versus Polydisperse Ultrasound Contrast Agents: In Vivo Sensitivity and safety in Rat and Pig. Ultrasound Med Biol. 2020 Dec;46(12):3339-3352. doi: 10.1016/j.ultrasmedbio.2020.07.031.
24. Segers T, Kruizinga P, Kok MP, Lajoinie G, de Jong N, Versluis M. Monodisperse Versus Polydisperse Ultrasound Contrast Agents: Non-Linear Response, Sensitivity, and Deep Tissue Imaging Potential. Ultrasound Med Biol. 2018 Jul;44(7):1482-1492. doi: 10.1016/j.ultrasmedbio.2018.03.019.
25. van Elburg B, et al. Dependence of sonoporation efficiency on microbubble size: An in vitro monodisperse microbubble study. J Control Release. 2023 Nov;363:747-755. doi: 10.1016/j.jconrel.2023.09.047.
26. Kanoulas E, et al. Super-Resolution Contrast-Enhanced Ultrasound Methodology for the Identification of In Vivo Vascular Dynamics in 2D. Invest Radiol. 2019 Aug;54(8):500-516. doi: 10.1097/RLI.0000000000000565.
27. van Hoeve W, et al. Improved Sensitivity of Ultrasound-Based Subharmonic Aided Pressure Estimation Using Monodisperse Microbubbles. J Ultrasound Med. 2022 Jul;41(7):1781-1789. doi: 10.1002/jum.15861.
28. Castro-Hernández E, van Hoeve W, Lohse D, Gordillo JM. Microbubble generation in a co-flow device operated in a new regime. Lab on a Chip. 2011;11(12):2023.
29. de Jong N, Hoff L, Skotland T, Bom N. Absorption and scatter of encapsulated gas filled microspheres: theoretical considerations and some measurements. Ultrasonics. 1992 Mar;30(2):95-103. doi: 10.1016/0041-624x(92)90041-j.
30. Kumar M.B., Sathiya P., Varatharajulu M. Selective Laser Sintering. BENTHAM SCIENCE PUBLISHERS eBooks. 2021 Nov 29;28–47.
31. Interventional [Internet]. Esaote.com. 2026 [cited 2026 Mar 3]. Available from: https://www.esaote.com/en-BE/interventional/probes
32. Song P, et al. Improved Super-Resolution Ultrasound Microvessel Imaging With Spatiotemporal Nonlocal Means Filtering and Bipartite Graph-Based Microbubble Tracking. IEEE Trans Ultrason Ferroelectr Freq Control. 2018 Feb;65(2):149-167. doi: 10.1109/TUFFC.2017.2778941.
33. Kuhn HW. The Hungarian method for the assignment problem. Naval Research Logistics [Internet]. 2005 Feb [cited 2020 Oct 10];52(1):7–21. Available from: https://web.eecs.umich.edu/~pettie/matching/Kuhn-hungarian-assignment.pdf
34. McCall JR, Santibanez F, Belgharbi H, Pinton GF, Dayton PA. Non-invasive transcranial volumetric ultrasound localization microscopy of the rat brain with continuous, high volume-rate acquisition. Theranostics. 2023 Feb 5;13(4):1235-1246. doi: 10.7150/thno.79189.

APPENDIX

Supplementary files

The manuscript presents a novel bi-disperse MB population, composed by two monodisperse MB populations. One population (p3MHz) is characterized by a strong non linear response, whereas the other MB population (p5.5MHz) mainly presents a fundamental response. To uncouple the bi-disperse MB population, the following equations are applied:

- h3MHz = h2, (Eq. 1)
- hp5.5MHz = h1 – h2. (Eq. 2)

where h3MHz and hp5.5MHz represent the images of the two uncoupled populations. H1 and h2 represent the images of the first and second harmonic after filtering by means of Fourier in the frequency domain of the MB signal.

In the supplementary files we present the results of individual injections and simultaneous injections. Experiments with individual injections serve as an initial validation for the uncoupling pipeline while having a ground truth. During single injections and in case of perfect uncoupling, the residual images, obtained by attempting to image the non-injected population, should be empty. On the other hand, simultaneous injections serve as a proof-of-concept of the separability when both MB populations are present.

Video 1 presents videos of singular injections of p3MHz. The video presents the results obtained before (a) and after (b) SVD filtering, and after uncoupling (c and d). In particular, (c) presents the results after applying equation Eq. 1 and (d) Eq. 2. In other words, in (c), we are imaging the population that is being injected (p3MHz) and in (d) we are imaging the residuals.

Video 2 presents videos of singular injections of p3MHz. The video presents the results obtained before (a) and after (b) SVD filtering, and after uncoupling (c and d). In particular, (c) presents the results after applying equation Eq. 2 and (d) Eq. 1. In (c), we are imaging the population that is being injected (p5.5MHz) and in (d) we are imaging the residuals.

Figure S1 shows the intensity projection obtained after simultaneous injections of the bi-disperse population. The colors code the two different MB populations.

Results of individual and simultaneous injections confirm the performance of the proposed uncoupling technique.

See the supplementary files on the website:
https://www.mattioli1885journals.com/index.php/theultrasoundjournal/article/view/18060